Influence of Stoichiometry and Aging at Operating Temperature on Thermoelectric Higher Manganese Silicides

Sylvain Le Tonquesse, Loïc Joanny, Quansheng Guo, Erik Elkaim, Valérie Demange, David Berthebaud, Takao Mori, Mathieu Pasturel, Carmelo Prestipino

Influence of stoichiometry and aging under operating temperature on thermoelectric Higher Manganese Silicides

Sylvain Le Tonquesse,[†] Loic Joanny,[‡] Quansheng Guo,[†] Erik Elkaim,[¶] Valérie Demange,[‡] David Berthebaud,[†] Takao Mori,[§] Mathieu Pasturel,[*,‡] and Carmelo Prestipino[*,‡]

†CNRS - Saint-Gobain - NIMS, UMI3629, Laboratory for Innovative Key Materials and Structures (LINK), National Institute for Materials Science, 1-1 Namiki, Tsukuba, Ibaraki 305-0044, Japan

‡Univ Rennes, CNRS, ISCR-UMR6226/ScanMAT-UMS2001, F-35000, Rennes, France

¶Synchrotron SOLEIL, L'Orme des Merisiers, BP 48, St Aubin, 91192 Gif sur Yvette, France

§National Institute for Materials Science (NIMS), WPI-MANA and CFSN, Tsukuba, Japan

E-mail: mathieu.pasturel@univ-rennes1.fr; carmelo.prestipino@univ-rennes1.fr

Abstract

Thermoelectric Higher Manganese Silicides, $MnSi_x$, were synthesized by magnesioreduction followed by spark plasma sintering with different nominal compositions (x = 1.65, 1.74, 1.80) and various post-synthesis annealing durations (0 h, 48 h, 96 h and 336 h). The composite Nowotny Chimney-Ladder crystal structures of the resulting samples were investigated by synchrotron X-ray powder diffraction. The modulation vector component γ, generally considered corresponding to the stoichiometry (x) of

the material, were accurately determined by Rietveld refinement using a (3+1)D superspace approach. Regardless of the initial nominal composition, all the samples have a similar $\gamma \sim 1.736$ after 48 h annealing at 900 K. This result suggests that $MnSi_x$, at the temperature of 900 K, is better described as a defined compound with x close to 1.736, rather than intermediate solid-solution phases with $1.725 < x < 1.75$ as predicted by the commonly accepted phase diagram. At the fixed nominal composition $MnSi_{1.74}$, γ increases significantly from 1.7313(2) to 1.7411(1) after 336 h annealing, indicating that the thermal history influences the Si stoichiometry. The evolution of γ with time is concomitant with a power factor drop (-19 %), attributed to a decrease of the charge carrier concentration. The drop of the power factor, partially compensated by a decrease of the thermal conductivity, results in a -12 % reduction of the maximum figure of merit ZT, after prolonged annealing under realistic application conditions.

1 Introduction

Thermoelectric (TE) generators are all-solid-state devices that enable the conversion of heat, including heat losses, into electricity thanks to the Seebeck effect. These generators most commonly consist in an assembly of *n*- and *p*-type TE materials connected electrically in series and thermally in parallel between two ceramic plates. The conversion efficiency of the device is directly proportional to the adimensional figure of merit $ZT = \alpha^2 T/\kappa\rho$ of the materials with α the Seebeck coefficient, ρ the electrical resistivity, κ the thermal conductivity and T the absolute temperature. Important research efforts have been undertaken during the past two decades to increase ZT of numerous materials such as Bi_2Te_3 [1], GeTe [2] or PdTe [3] to enable a more extensive development of the TE technology. However, many other factors must be taken into account when selecting materials for TE generator, such as the raw material costs and toxicity [4], mechanical properties, chemical and thermal stability, and thermal expansion coefficients [5]. For all these reasons, Higher Manganese Silicides (HMS) with composition $MnSi_x$ ($1.725 < x < 1.75$) are considered as promising

p-type thermoelectric materials for the mid-temperature applications (600 - 800 K), despite a moderate ZT of 0.4[6].

By Miyasaki *et al.*[7], HMS crystallize in a tetragonal composite crystal Nowotny chimney-ladder structure-type as shown in Fig. 1. It consists of the interpenetration of a [Si] and a [Mn] subsystems with equal a cell parameter but different and incommensurate c parameters *i.e.* with an irrational ratio. Because both subsystems have 4 atoms per unit cells, the ratio $c_{Mn}/c_{Si} = \gamma$, corresponds to the Si stoichiometry of the compound x. HMS structure is described as an incommensurate composite crystal using the (3+1)D superspace approach[7] which symmetry is described by $I4_1/amd(00\gamma)00ss$ space group and the reciprocal lattice is indexed using two $\boldsymbol{a}^* = \boldsymbol{b}^*$ vectors having conventional 2D periodicity and two additional collinear vectors, $\boldsymbol{c}^*_{Mn}$ and $\boldsymbol{c}^*_{Si}$, linked by the relation $\|\boldsymbol{c}^*_{Si}\| = \gamma \|\boldsymbol{c}^*_{Mn}\|$[8]. Such a super-space approach has the advantage to describe correctly and with the same degree of precision, all the stoichiometries in the range of stability, and finally evaluate γ, and thus x, from cell metric determination.

A good understanding of the intrinsic structure-properties relationship of HMS is difficult to establish due to their high structural and microstructural complexity. For example, metallic MnSi planar inclusions are formed inside the HMS grain of materials prepared by direct solidification of a melt which can strongly effect the measured properties. In addition, MnSi or Si secondary phase are almost always present in materials synthesized by conventional fusion/solidification routes due to the high vapor pressure and the peritectic formation of $MnSi_x$. For these reasons, the influence of the synthesis conditions on x remains unclear as some studies claim that the Si stoichiometry can be controlled by adjusting the initial nominal composition[9] whereas others results seem to indicate that the thermal history of the sample has a stronger influence[10,11]. High temperature XRD has shown that while γ remains stable up to 1173 K, it then rapidly decreases up to the decom-

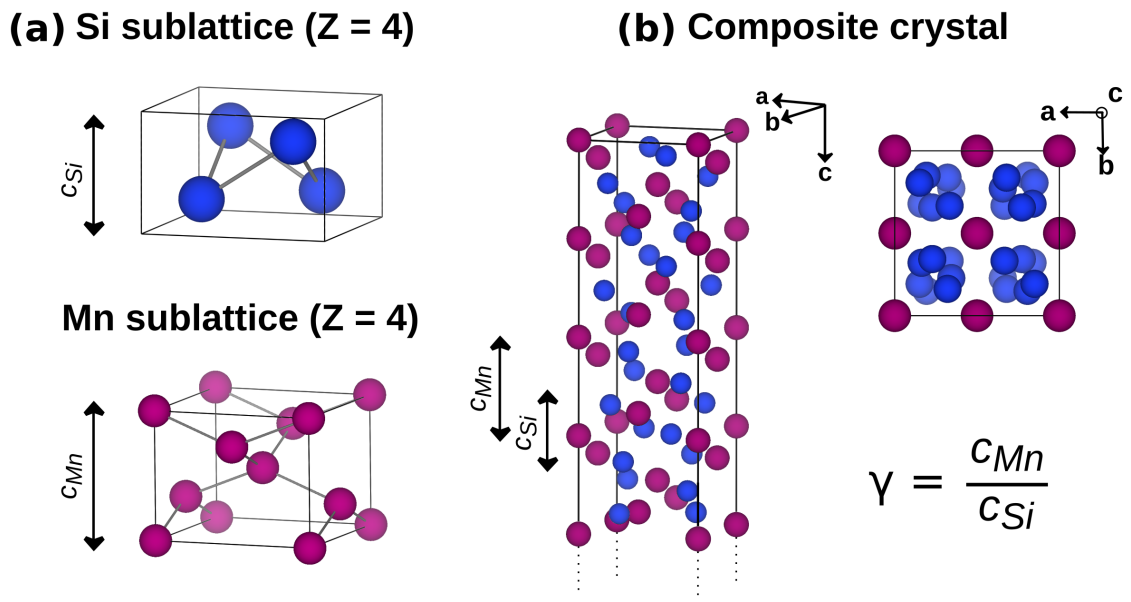

Figure 1: (a) Representation of the [Mn] and [Si] subsystems and (b) of the composite crystal structure of $MnSi_\gamma$ after interpenetration of the two subsystems.

position point of $MnSi_x$ [12]. However, Pichon *et al.* showed that the γ and TE performances of HMS made by 'ribbon growth on substrate' synthesis decrease within few hours upon annealing in air at the temperature of 873 K, due to structural evolution [13]. Better knowledge of the influence of the synthesis conditions as well as the high-temperature aging on the intrinsic properties of HMS must be gained to better design and predict the conversion efficiency of TE modules.

In this study, a set of HMS samples were synthesized by magnesioreduction, as this process offers the advantage to produce highly pure HMS without MnSi inclusions [14]. The influence of the nominal Si stoichiometry and annealing conditions on the structure, and especially of the modulation γ, were investigated by synchrotron X-ray diffraction. The highly intense synchrotron radiation enables high statistic of measurement over a large fraction of the reciprocal space which is indispensable to detect many weak incommensurate peaks carrying the information about the modulation of the atoms in HMS. The evolution of the TE properties upon prolonged annealing at 800 K, which is of high prac-

tical importance, are discussed in terms of possible structural and microstructural changes in the material.

2 Experimental procedure

The magnesioreduction (MR) synthesis of $MnSi_x$, with x = 1.65, 1.74 and 1.80, starting from MnO (Alfa Aesar, 99 %) and Si (Ventron, 99.9 %) is described in details in previous articles[14,15]. The reaction temperature of 1173 K was reached at a rate of 60 K h^{-1} and held for 8 h before being cooled down by switching off the furnace. The MgO by-product is removed by soaking the as-synthesized powder twice in diluted hydrochloric acid ($\sim$ 0.2 N) for 5 minutes and washing three times in distilled water and once more in ethanol before being dried at 353 K overnight. The washed $MnSi_\gamma$ powder was densified by spark plasma sintering (SPS) in Ø 10 mm graphite dies at 1273 K and 75 MPa for 30 min with 100 K min^{-1} heating/cooling rates using a FCT HP-D-10 apparatus. All sintered samples have a relative density of about 95 %. The samples were annealed under residual Ar atmosphere in sealed silica tubes for different durations and temperature conditions (see Table 1), before being quenched in cold water. In the case of $MnSi_{1.74}$-96h, the sample was produced by annealing the bar-shaped piece of $MnSi_{1.74}$-0h used for the transport properties measurement and not independently following the procedure described above. For this reason, the thermal diffusivity measurement, which required a pellet-shaped sample, were not measured for $MnSi_{1.74}$-96h.

Scanning electron microscopy (SEM) images and electron back-scattering diffraction (EBSD) maps were realized using a JEOL JSM 7100F instrument apparatus equipped with an EBSD HKL Advanced Nordlys Nano detector. EBSD data were collected using an incident electron beam of 20 kV and a step width of 50 nm over an area of about 20 x 10 μm^2. The Kikuchi patterns were successfully indexed using the unit cell of the commensurate [Mn] subsystem (space group $I4_1/amd$, $a \sim 5.52$ Å, $c \sim 4.37$ Å). For the determination of

Table 1: Nominal compositions and annealing conditions used for the investigated HMS samples.

Sample name	Nominal composition	Annealing conditions
$MnSi_{1.65}$ - 48h	$MnSi_{1.65}$	48 h at 900 K
$MnSi_{1.74}$ - 48h	$MnSi_{1.74}$	48 h at 900 K
$MnSi_{1.80}$ - 48h	$MnSi_{1.80}$	48 h at 900 K
$MnSi_{1.74}$ - 0h	$MnSi_{1.74}$	no annealing
$MnSi_{1.74}$ - 96h	$MnSi_{1.74}$	96 h at 800 K *
$MnSi_{1.74}$ - 336h	$MnSi_{1.74}$	336 h at 800 K

* prepared from sample $MnSi_{1.74}$-0h

the crystallites size distribution, only diffracting domains of at least 12 pixels (*i.e.* ~ 0.03 μm^2) were considered, and their size was defined as the diameter of a circle with an equal surface.

The X-ray diffraction measurements were carried out on CRISTAL beamline at SOLEIL synchrotron (Saint-Aubin, France), using the 2-circle diffractometer (capillary Debye–Scherrer geometry) equipped with a new 50 degrees detection system composed by a set of 9 1D microstrip photon counting detectors (Mythen2X from Dectris Ltd. -Switzerland). The sintered pellets were finely crushed using a WC mortar and the powder was filled in borosilicate capillaries ($\O$ = 0.3 mm). Incident X-ray beam with wavelength of λ = 0.58143 Å (refined using a LaB_6 NIST standard) was selected using a Si(111)-double crystal monochromator from an undulator source. Structural parameters were determined by Rietveld refinement of the XRD patterns using the software JANA2006[16]. The anisotropic broadening affecting the Si (*hk0m*) and satellite (*hklm*) reflections was modeled using a generalized Stephan's method[17] for incommensurate structure[18]. More realistic estimated standard deviation were obtained using the Berar's method[19]. The amount of secondary phase was determined by Rietveld quantitative analysis.

Thermal diffusivities (D) were measured on $\O$ = 10 mm and $\sim$ 2 mm thick samples

coated with graphite using a Netzsch LFA 467 HyperFlash apparatus under N_2 atmosphere. The thermal conductivity was calculated using the relation $\kappa = D \times C_p \times d$ where C_p is the specific heat of the sample determined using a Netzsch Pyroceram reference sample and d is the sample density measured by the Archimede method. The electrical resistivity and Seebeck coefficient were measured simultaneously on $6 \times 2 \times 2$ mm^3 shaped bars using a ZEM2 apparatus (ULVAC-RIKO Inc.) under He atmosphere.

3 Results and discussion

3.1 Synchrotron powder X-ray diffraction

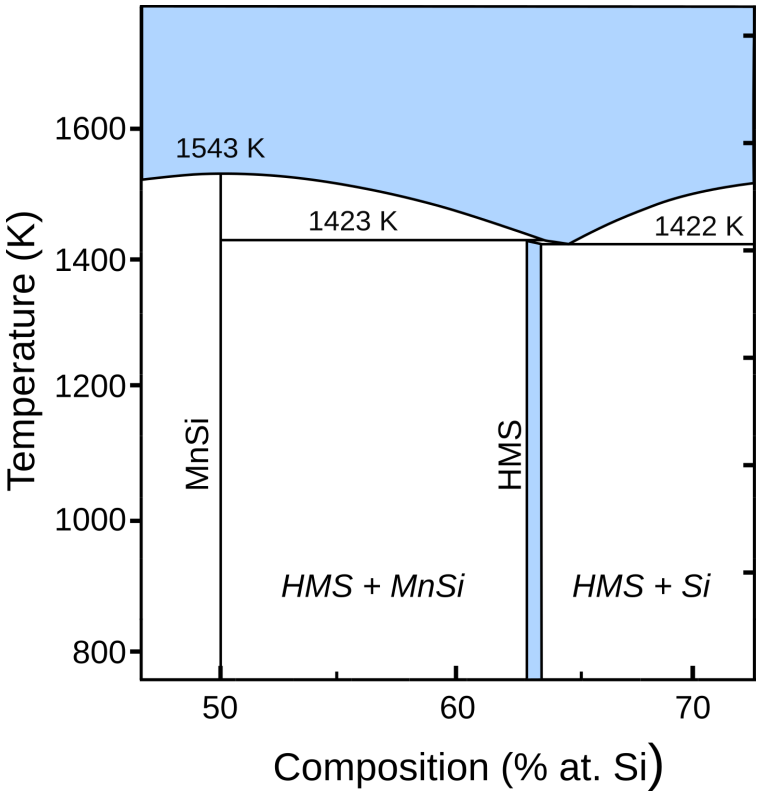

Figure 2: Si-rich part of the Mn-Si phase diagram according to ref.[20].

According to the commonly accepted Mn-Si phase diagram (Fig. 2), HMS has a homogeneity range between $MnSi_{1.725}$ (63.3 at. % of Si) and $MnSi_{1.75}$ (63.6 at. % of Si) up to the peritectic decomposition at 1423 K[20].Outside this composition range, the HMS phase

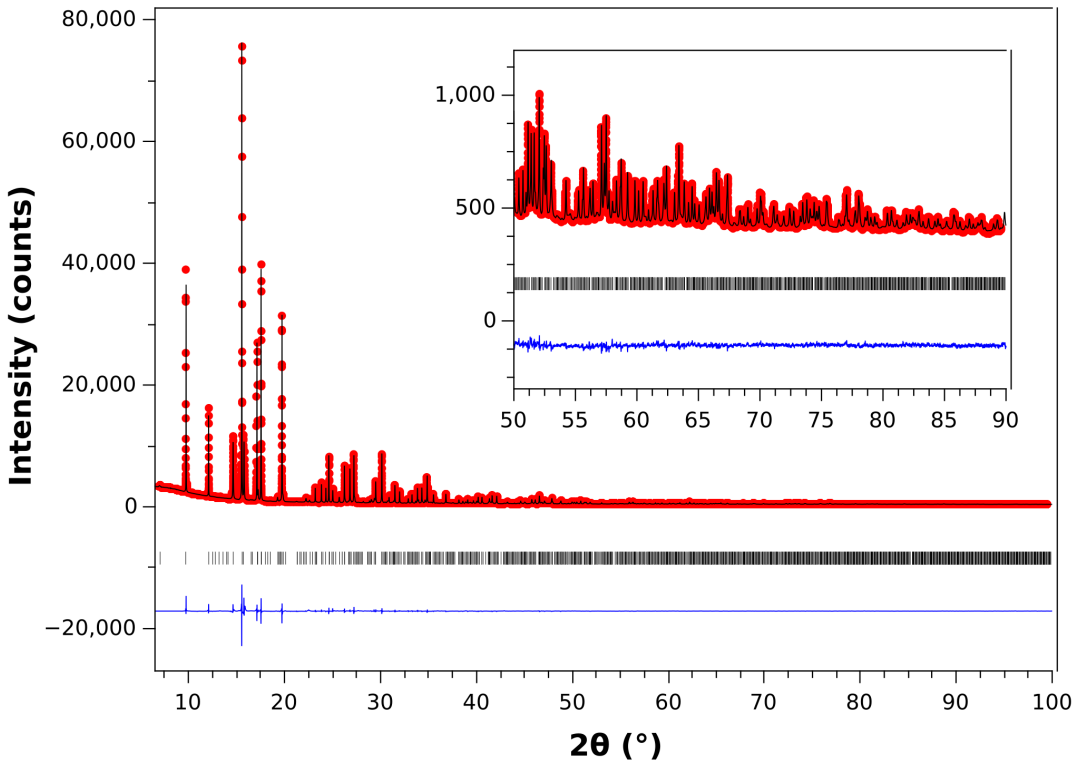

Figure 3: Rietveld refined synchrotron powder XRD pattern of $MnSi_{1.74}$-48h (λ = 0.58143 Å). The experimental data are plotted in red symbols, the calculated pattern with a black line and the difference with a blue line. The vertical ticks indicate the theoretical Bragg positions. The inset is a magnified view of the high angular region of the refined pattern.

is in thermodynamic equilibrium with MnSi and Si, respectively. According to the composite crystal structural model described above, the value of γ could therefore be controlled by adjusting the nominal composition of the materials during the synthesis. In order to check this prediction, the samples $MnSi_{1.65}$-48h, $MnSi_{1.74}$-48h and $MnSi_{1.80}$-48h, were prepared using identical magnesioreduction/SPS/annealing conditions.

The three samples were investigated by synchrotron powder XRD and the patterns fitted using the above described (3+1)D structural model of HMS (Fig. 3 and Fig. SI 1). It worth of noticing the high cristallinity of the phases synthesized by magnesioreduction, peaks remain very sharp also at angles higher than 85 degrees, corresponding to Q =

14.60 $Å^{-1}$. Refined parameters and R-factors are given in Table 2. The Bragg R-factors were around 3 % for all the compositions indicating a reasonable structural model, while the larger χ^2 of the samples were attributed to the high statistic of measurements[21]. As expected from the phase diagram, MnSi (18 wt. %) and Si (1 wt. %) impurity are visible on the XRD patterns of $MnSi_{1.65}$-48h and $MnSi_{1.80}$-48h, respectively (Fig. 4). $MnSi_{1.74}$-48h is single phase as all the visible Bragg peaks are fully indexed with the HMS structure. Moreover, elemental Mn and Si EDS maps confirm the high chemical homogeneity of $MnSi_{1.74}$-48h and a composition Mn : Si close to 1 : 1.75 (Fig. SI 2).

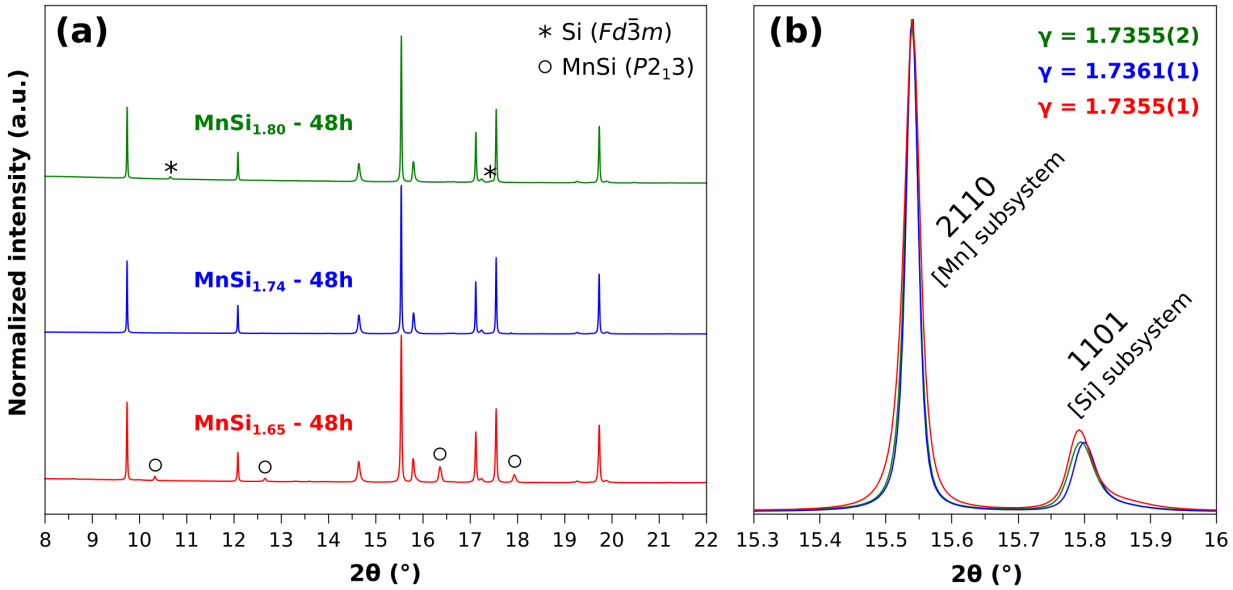

Figure 4: (a) low angular region of the normalized XRD patterns of $MnSi_{1.65}$-48h (red), $MnSi_{1.74}$-48h (blue) and $MnSi_{1.80}$-48h (green). (b) Magnified view of the XRD patterns aligned on the (2110) reflection and showing the absence of significant shift of the (1101) reflection with increasing Si content.

Surprisingly, the patterns of the 3 samples are very similar and the γ values determined by Rietveld refinement are all around 1.736. From the phase diagram, one would expect to find γ close to 1.725 and 1.75 for the samples $MnSi_{1.65}$-48h and $MnSi_{1.80}$-48h, respectively. The absence of significant evolution can be visually evaluated in Fig. 4 where a close-up view of the (2110) and the (1101) Bragg peaks relative to the [Mn] subsystem and the

[Si] subsystem are represented. Any significant change of γ among the samples would lead to a significant shift of the (1101) peak since $c_{Mn} = \gamma\, c_{Si}$. All other structural parameters such as the common a parameter, the Fourier amplitudes of the modulation functions and atomic displacement parameters are similar regardless of the initial nominal composition. The present results indicate that at a given temperature, $MnSi_x$ is better described as a defined composition with $x \sim 1.736$ rather than an intermediate solid-solution with $1.725 < x < 1.75$, in such case the differences the γ value present in literature should be ascribed to a different origin than the initial composition.

Table 2: Structural parameters, phase fractions and R-factors obtained by Rietveld refinement of $MnSi_{1.65}$-48h, $MnSi_{1.74}$-48h and $MnSi_{1.80}$-48h XRD patterns.

	$MnSi_{1.65}$-48h	$MnSi_{1.74}$-48h	$MnSi_{1.80}$-48h
γ	1.7355(2)	1.7361(1)	1.7355(1)
a (Å)	5.5259(3)	5.5264(2)	5.5265(2)
[Mn] subsystem			
$\bar{x}, \bar{y}, \bar{z}$	0, 0, 0	0, 0, 0	0, 0, 0
c_{Mn} (Å)	4.3674(3)	4.3672(2)	4.3675(2)
V_{Mn} (Å^3)	133.36(2)	133.38(1)	133.39(1)
B_z^2	-0.0180(8)	-0.0188(5)	-0.0181(7)
B_z^4	0.005(3)	0.003(2)	0.005(2)
U_{iso} (Å^2)	0.0041(3)	0.0039(2)	0.0049(2)
[Si] subsystem			
$\bar{x}, \bar{y}, \bar{z}$	0.25, 0.25, 0.25	0.25, 0.25, 0.25	0.25, 0.25, 0.25
c_{Si} (Å)	2.5165(6)	2.5155(3)	2.5166(3)
V_{Si} (Å^3)	76.84(3)	76.82(2)	76.86(2)
A_x^1	0.0767(4)	0.0770(3)	0.0768(3)
A_x^3	-0.0106(5)	-0.0107(3)	-0.0106(3)
B_z^4	-0.042(2)	-0.042(2)	-0.041(2)
A_x^5	-0.0030(7)	-0.0030(5)	-0.0029(5)
U_{iso} (Å^2)	0.0060(5)	0.0060(3)	0.0065(4)
Phase fractions (wt. %)			
$MnSi_\gamma$	81.8(8)	100	99(2)
MnSi	18.2(4)	0	0
Si	0	0	1(1)
R-factors			
χ^2	21.16	17.72	7.84
R_B	2.98	2.99	3.94

The XRD patterns of HMS samples with nominal composition $MnSi_{1.74}$ aged at 800 K for 0 h, 96 h, and 336 h are shown in Fig. 5. This annealing temperature was selected because it corresponds to best performances in the operating range of undoped HMS. For every aging time, all Bragg peaks could be indexed with the HMS phase indicating the high purity of the samples and the absence of decomposition. Rietveld refined patterns and refined structural parameters are given in Fig. SI 3 and Table 3, respectively. Interestingly, a clear increase of γ is observed with increasing annealing time. The γ value of as-sintered $MnSi_{1.74}$-0h increases from 1.7312(2) to 1.7403(2) after 4 days and then to 1.7411(1) after 2 weeks annealing. The increase of γ is due to a significant shortening of c_{Si} going from 2.5238(5) Å without annealing to 2.5087(3) Å after 336 h of annealing whereas c_{Mn} remains constant over time. The evolution of γ over annealing time is clearly visible on the XRD pattern in Fig. 5 with the large shift of the (1101) peak toward higher angles. It should also be noticed that a parameter, common to both subsystems, increases from 5.5256(5) Å to 5.5291(4) Å after 336 h. This may result from lattice strain release along the (a,b) plane caused by the shortening of the [Si] unit cell along the c axis. Otherwise, all Fourier amplitudes of the modulation functions and atomic displacement parameters remain similar for all samples.

This result shows that as-sintered $MnSi_{1.74}$-0h is not thermodynamically stable at 800 K and also at such temperature the structural evolution kinetic is slow, as γ continues to increase significantly even after 4 days annealing. Moreover, Kikuchi *et al.* studied, by *in situ* high-temperature XRD, the thermal evolution of γ in HMS [12], showing that γ remains constant around 1.739 up to 800 K before decreasing linearly down to about 1.725 just before reaching the decomposition point. The emerging figure coming from the critical examination of the Kikuchi *et al.* and the present studies it is that HMS samples are generally sintered or synthesized at high temperature (above 800 K), where kinetic are fast, and cooled down rapidly (100 K min^{-1} for SPS), it can be assumed that γ is kinetically trapped

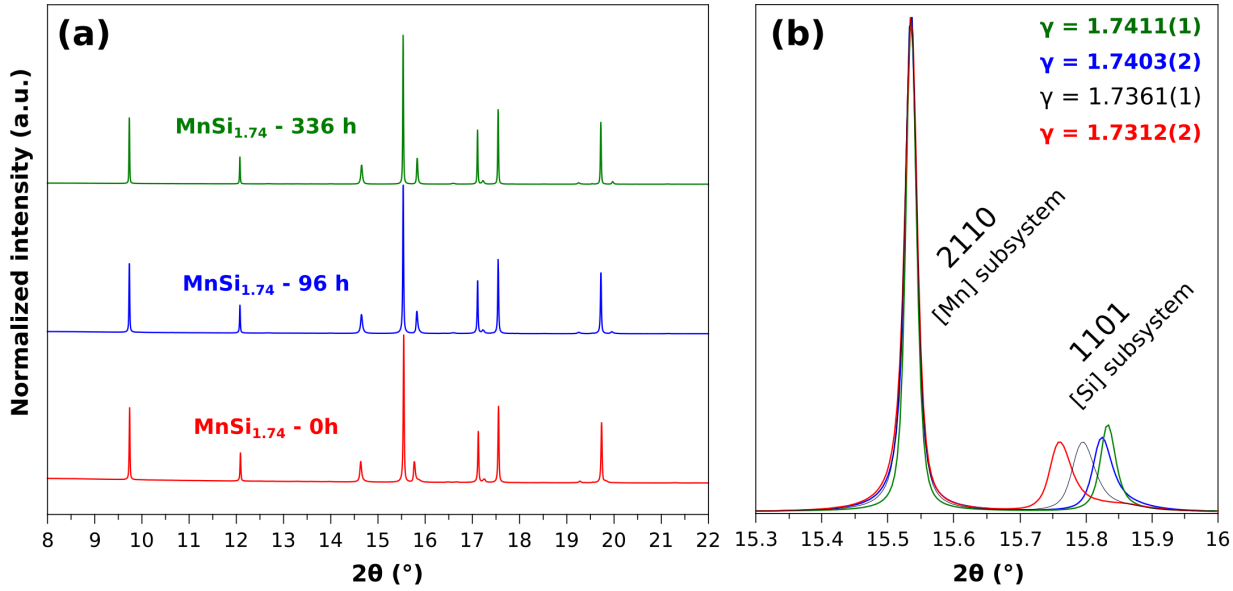

Figure 5: (a) low angular region of the normalized XRD patterns of the samples $MnSi_{1.74}$-0h (red), $MnSi_{1.74}$-96h (blue) and $MnSi_{1.74}$-336h (green). (b) Magnified view of the XRD patterns aligned on the 2110 reflection and showing the shift of the 1101 reflection with increasing annealing time. The black XRD pattern in (b) corresponds to the sample $MnSi_{1.74}$-48h.

to a low value in as-sintered HMS. This is in agreement with the low γ value of 1.7313(2) determined by XRD for $MnSi_{1.74}$-0h. Upon annealing at 800 K, the HMS slowly tend towards thermodynamic equilibrium with γ close to 1.74 as determined for $MnSi_{1.74}$-96h and $MnSi_{1.74}$-336h. As shown in Fig. 6, similar behaviors were reported in other studies in which as-sintered pellets or as-cast ingots always show low γ around 1.73 which increase upon long annealing below 873 K[10,11,13].

Notice that γ of 1.7411(1) determined for $MnSi_{1.74}$-336h in the present work is significantly higher than γ of 1.7387(1) determined by Kikuchi *et al.* in their study. It can be explained by the slow kinetic that makes sample with $\gamma > 1.74$ unreachable within the time span of a conventional XRD measurement that usually last a few hours. In many articles, the thermoelectric properties of HMS are reported on as-sintered or as-cast samples. According to the present results, such samples are not representative of the material in op-

Table 3: Structural parameters and R-factors obtained by Rietveld refinement of $MnSi_{1.74}$-0h, $MnSi_{1.74}$-96h and $MnSi_{1.74}$-336h XRD patterns.

	$MnSi_{1.74}$-0h	$MnSi_{1.74}$-96h	$MnSi_{1.74}$-336h
γ	1.7313(2)	1.7403(2)	1.7411(1)
a (Å)	5.5256(5)	5.5294(4)	5.5291(4)
[Mn] subsystem			
$\bar{x}, \bar{y}, \bar{z}$	0, 0, 0	0, 0, 0	0, 0, 0
c_{Mn} (Å)	4.3678(4)	4.3673(1)	4.3678(3)
V_{Mn} (Å^3)	133.36(3)	133.56(2)	133.52(2)
B_z^2	-0.0175(7)	-0.0187(6)	-0.0184(5)
B_z^4	0.004(1)	0.005(2)	0.005(1)
U_{iso} (Å^2)	0.0039(2)	0.0041(2)	0.0038(2)
[Si] subsystem			
$\bar{x}, \bar{y}, \bar{z}$	0.25, 0.25, 0.25	0.25, 0.25, 0.25	0.25, 0.25, 0.25
c_{Si} (Å)	2.5238(5)	2.5095(3)	2.5087(3)
V_{Si} (Å^3)	77.03(3)	76.73(2)	76.69(2)
A_x^1	0.0770(4)	0.0771(4)	0.0769(3)
A_x^3	-0.0106(4)	-0.0108(4)	-0.0106(3)
B_z^4	-0.041(2)	-0.042(2)	-0.041(2)
A_x^5	-0.0028(6)	-0.0032(6)	-0.0032(4)
U_{iso} (Å^2)	0.0058(5)	0.0065(5)	0.0056(4)
R-factors			
χ^2	12.74	20.79	23.13
R_B	3.21	3.31	3.05

erating condition, the thermal history of the sample has a high impact on the HMS crystal structure. Better understanding of the effect of γ on the thermoelectric properties is thus required to better predict the real behavior of HMS under optimal operating temperatures and a more critical approach to synthesis approach.

3.2 Microstructure

Apart from the crystal structure, the microstructure of polycrystalline materials may have an important effect on the final macroscopic properties. For example, increasing the grain boundaries density by nanostructuration or formation of nanoinclusions have been successfully used to decrease the lattice thermal conductivity and thus increase the perfor-

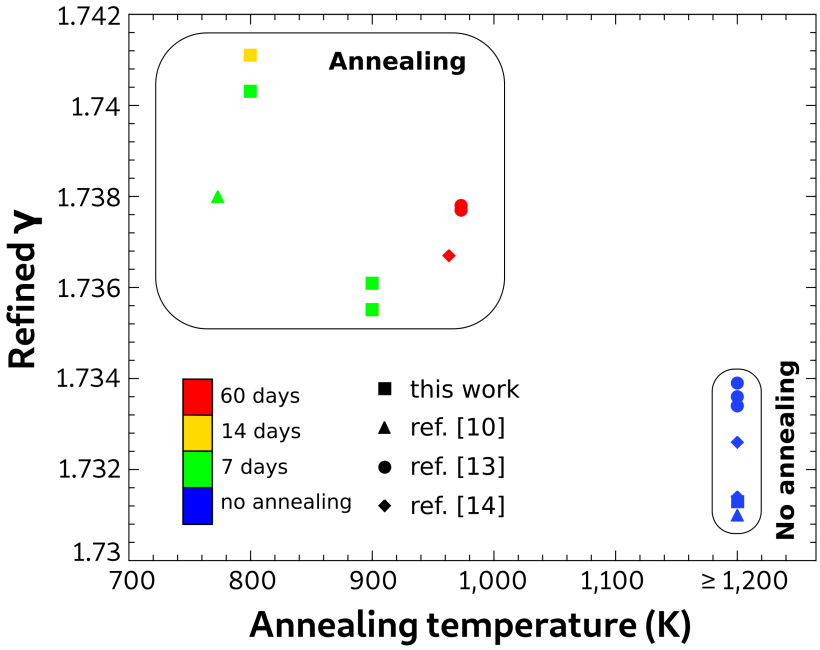

Figure 6: Influence of the annealing on the value of γ determined by XRD refinement for samples from the literature synthesized by arc-melting, powder synthesis/SPS or 'ribbon grown on substrate' routes.

mance of many thermoelectric materials. The charge carrier mobility and consequently the electronic properties may also be impacted by such nanostructuration. For high temperature applications, the stability of the microstructure under application conditions is of uppermost importance to enable the long term stability of the performances. For such reasons, we have investigate the effect of the long annealing on the microstructure and check if the difference in thermoelectric properties could be ascribed to a microstructure effect and not to the variation of γ. SEM backscattered electron images and EBSD maps of samples $MnSi_{1.74}$-0h and $MnSi_{1.74}$-336h are shown in Fig. 7. In both cases, the majority of the diffracting pixels were well indexed with the HMS structure confirming the good purity of the samples. No texturation could be detected and the samples are therefore considered as isotropic. Computational determination of the diffracting areas surface enables the estimation of the crystallite size distributions. Both distributions were well fitted by a log-normal law with the average size value and the standard deviation as free param-

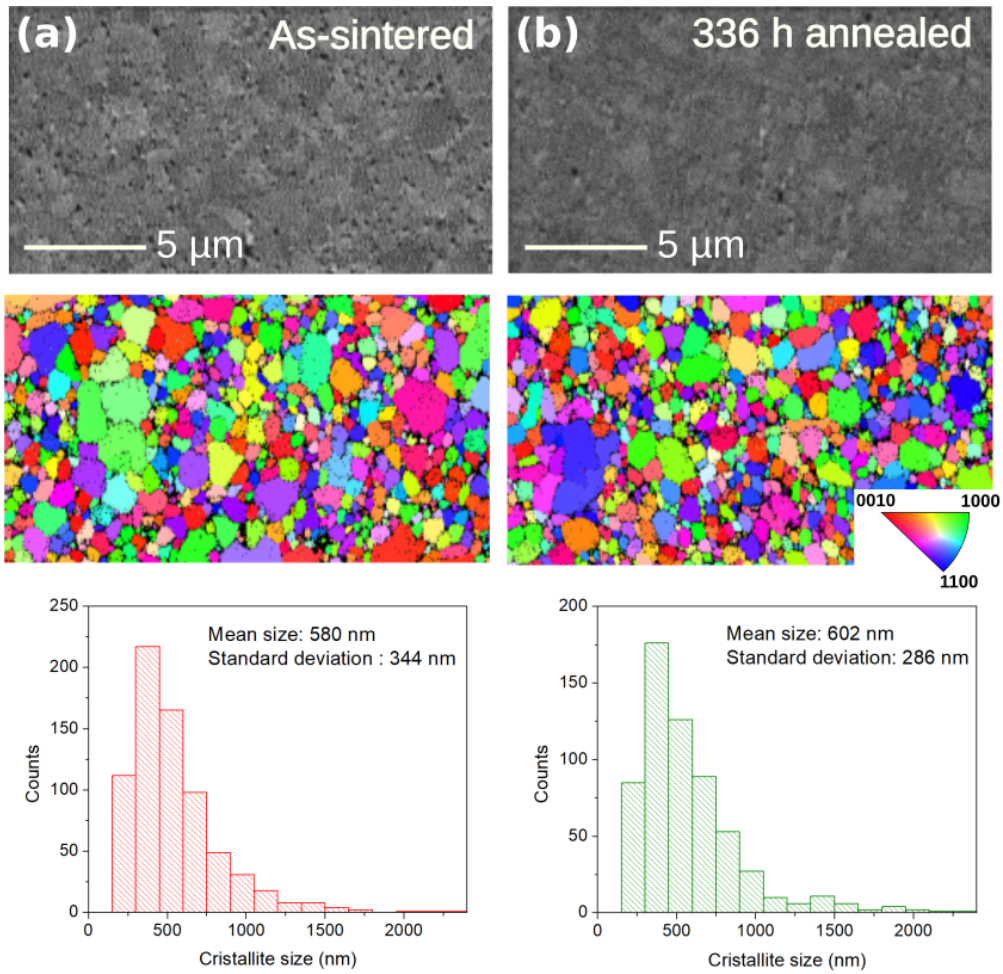

Figure 7: SEM backscattered electron images, EBSD analyses and crystallite size distribution of (a) $MnSi_{1.74}$-0h and (b) $MnSi_{1.74}$-336h samples.

eters. Upon 336 h annealing, the average size negligibly increases from 580 to 602 nm and the distribution becomes slightly narrower. Such small evolution of the microstructure is expected to have a negligible effect on the macroscopic thermoelectric properties. In the present case, the effect of annealing on the thermoelectric properties are thus only attributed to the structural evolution determined by XRD.

3.3 Thermoelectric properties

Fig. 8a and b show the thermal evolution of electrical resistivity and Seebeck coefficient, respectively, of $MnSi_{1.74}$-0h (red), $MnSi_{1.74}$-96h (blue) and $MnSi_{1.74}$-336h (green). The measurement of $MnSi_{1.74}$-0h was cycled twice and the data are shown with filled symbols

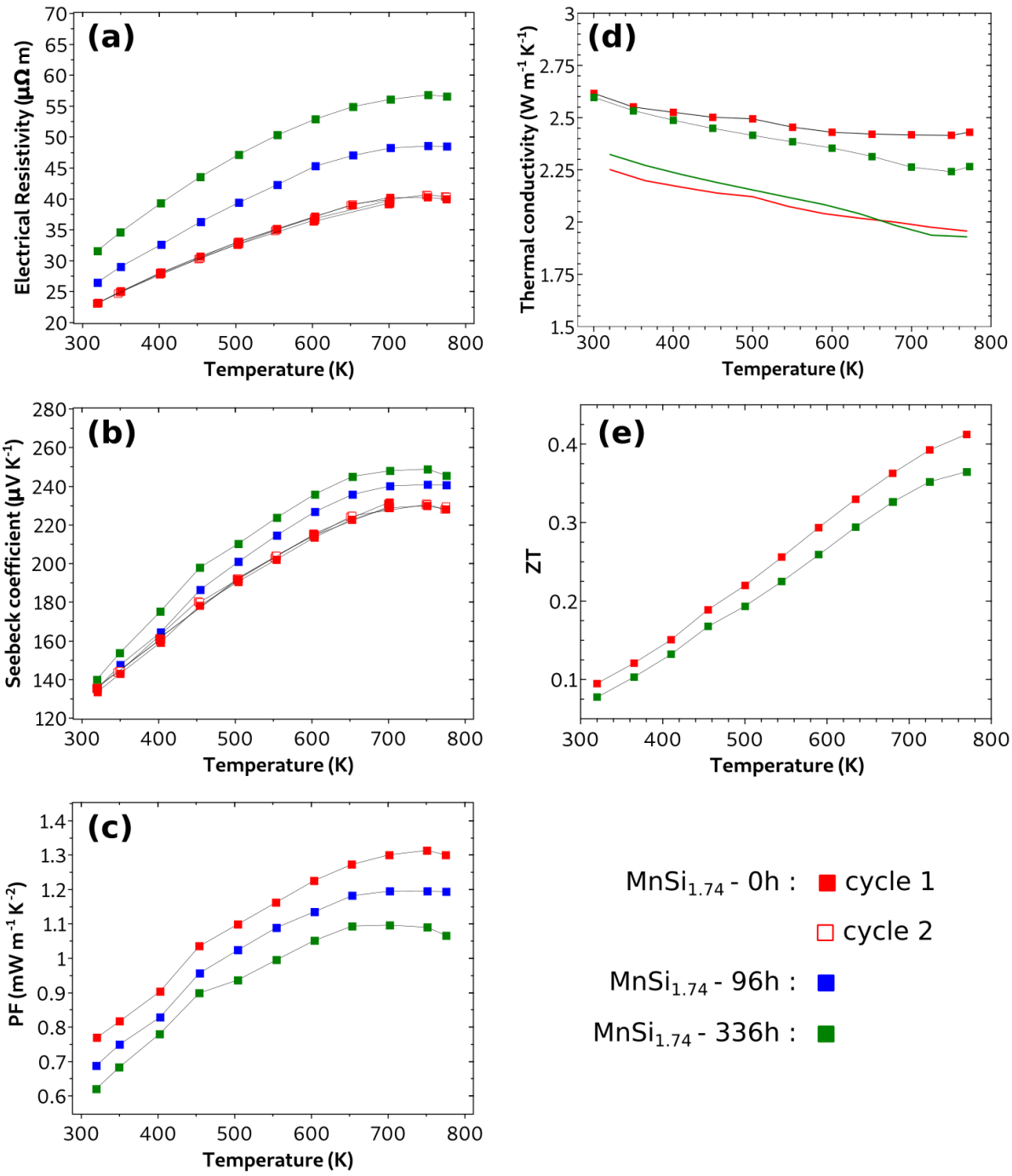

Figure 8: High temperature thermoelectric properties of $MnSi_{1.74}$-0h (red), $MnSi_{1.74}$-96h (blue) and $MnSi_{1.74}$-336h (green): (a) electrical resistivity, (b) Seebeck coefficient, (c) power factor, (d) total (symbols) and lattice (solid lines) thermal conductivities and (e) figure-of-merit ZT. Two measurement cycles (filled and empty symbols) are represented in (a) and (b) for $MnSi_{1.74}$-0h showing the good stability of the TE properties over short thermal cycling.

for the first run and empty symbols for the second run. The reversibility of the measurement seems to indicate a good thermal stability of the material upon thermal cycle. However, it becomes clear with $MnSi_{1.74}$-96h and $MnSi_{1.74}$-336h that after long annealing the transport properties of the sample evolve significantly. At 773 K, ρ increases from 40 to 48 $\mu\Omega$ m and then 57 $\mu\Omega$ m after 336 h annealing. This represents an increase of about 45 % of the electrical resistivity. Simultaneously, the Seebeck coefficient at 773 K continuously increases from 227 to 244 μV K^{-1}. As a result, the power factor (PF), shown in Fig. 8c, drops by 19 % from 1.30 to 1.05 mW m^{-1} K^{-2}. The TE properties of $MnSi_{1.74}$-0h are in good agreement with literature data on as-sintered undoped HMS prepared by more conventional synthesis methods such as arc-melting[22] or solid-state reaction[23]. Relatively high PF of about 1-3 to 1.5 mW m^{-1} K^{-2} are also obtained at 800 K for these sintered materials which were no annealed before measurements. Similarly to γ, the properties of HMS are much less affected by the synthesis method that the thermal history of the sample.

The degradation of the electronic properties upon annealing is attributed to the structural evolution described above and more particularly to the increase of γ. The band structure of Mn_4Si_7 ($\gamma = 1.75$), $Mn_{27}Si_{47}$ ($\gamma \sim 1.741$), $Mn_{15}Si_{26}$ ($\gamma \sim 1.733$) and $Mn_{11}Si_{19}$ ($\gamma \sim 1.727$) was calculated by means of first principles calculations by Migas *et al.*[24]. The authors reported that all the compositions have similar band structure with a indirect band-gad of about 0.7 eV. The Fermi level is found just above the valence band in the band gap for Mn_4Si_7 predicting a semiconductor behaviour. For the other compositions, the Fermi level is found to decreasing monotonously with γ inside the valence band resulting in degenerated semiconductors. Calculations predict an increase of the charge carrier concentration n from 1.1×10^{21} to 2.7×10^{21} going from $\gamma \sim 1.741$ to ~ 1.727, respectively. A more general correlation between γ and n was proposed by Fredrickson *et al.* and Imai *et al.* for chimney-ladder phases[25,26]. They phases are expected to behave as intrinsic semiconductors with a valence electron count (VEC) of 14. The VEC of HMS can be calculated

as follow:

$$VEC = 7 + 4\gamma \approx 13.9 \quad (1)$$

with 7 and 4 corresponding to the valence electron of Mn ($3d^5\ 4s^2$) and Si ($3s^2\ 3p^2$), respectively. This relatively simple rule successfully predicts the *p*-type conduction of HMS whose VEC > 14. A estimation of n can be predicted using the relation:

$$n = 4\ \frac{14 - VEC}{V_{Mn}} \quad (2)$$

with 4 corresponding to the formula unit in the [Mn] unit cell and V_{Mn} (cm^3) to the [Mn] unit cell volume. According to relations (1) and (2), the charge carrier concentration in the sample $MnSi_{1.74}$-0h and $MnSi_{1.74}$-336h would be 2.25 10^{21} and 1.08 10^{21} cm^{-3}, respectively. This value of charge carrier concentration are in very good agreement with those calculated by Migas *et al.* from band structure calculations[24] and experimental values reported HMS[13,27,28]. In first approximation, the electrical resistivity ρ can be linked to n by the relation:

$$\rho = \frac{1}{n \cdot \mu \cdot e} \quad (3)$$

with μ the charge carrier mobility and e the electron charge, while the Seebeck coefficient α can be estimated by the Pisarenko relation:

$$\alpha = \frac{8\pi^2 k_B^2 T}{3eh^2} \cdot m^\star \cdot (\frac{\pi}{3n^{2/3}} \quad (4)$$

with k_B the Boltzmann constant, h the Planck constant and $m^\star$ the effective mass of the charge carriers. The expected drop of n caused by the increase of γ is expected to play an important role in the simultaneous increase of ρ and α upon annealing.

The measured thermal conductivity κ (filled symbols) and the calculated lattice thermal conductivity κ_L (lines) of $MnSi_{1.74}$-0h and $MnSi_{1.74}$-336h are shown in Fig. 8d. κ_L was determined by subtracting the electronic contribution κ_e, calculated using the Wiedemann-Franz relationship $\kappa_e = \mathrm{L}\times\mathrm{T}/\rho$ with $\mathrm{L} = 2.4\ 10^{-8}\ \mathrm{W}\ \Omega\ \mathrm{K}^{-2}$, to the total thermal conductivity. The effect of annealing seems to have a weak effect on κ_L as both samples have similar values on the whole temperature range measured. However, due to its significantly higher electrical resistivity, and thus lower κ_e, $MnSi_{1.74}$-336h has κ approximately 10 % lower than $MnSi_{1.74}$-0h around 773 K. The maximum ZT of $MnSi_{1.74}$-0h is about 0.41 at 773 K which is in agreement with most literature data for undoped HMS. However, the large decrease of PF after 336 h annealing, lowers the maximum ZT down to 0.36 at 773 K.

4 Conclusion

This work presents a synchrotron powder X-ray diffraction study of two sets of $MnSi_x$ samples synthesized by magnesioreduction. In the first set of samples, $MnSi_x$ were prepared with different nominal composition (x = 1.65, 1.74 and 1.80) and annealed at 900 K for 48 h. Single phase HMS was obtained for x = 1.74 while MnSi and Si secondary phases were observed for x = 1.65 and 1.80, respectively. Similar modulation vector component $\gamma \sim 1.736$, which is related to the genuine Si stoichiometry x of the materials, were determined by Rietveld refinement. This reveals that the commonly accepted Mn-Si phase diagram is incorrect. Instead of being an intermediate solid-solution, $MnSi_x$ is more correctly described as a defined compound with x $\approx$ 1.736 at 900 K. In the second set of samples, HMS with nominal composition $MnSi_{1.74}$ were annealed at 800 K for different times (0 h, 96 h, 336 h). The heat treatments influence significantly γ which goes from

1.7313(2) to 1.7411(1) after 336 h at 800 K. Such structural evolution affects directly the electronic band structure of the material and especially the charge carrier concentration which is expected to drop. It results in a higher electrical resistivity (+45 %), a higher Seebeck coefficient (+7 %) and a significantly lower PF (-19 %) for the sample annealed for the longest time. However, the effect on ZT is partially compensated by the reduction of κ_e resulting in a -12 % decrease of the maximum ZT.

The present results show that γ is function of the temperature but the structural transition is kinetically slow below 800 K, meanings that past comparisons of HMS synthesized through different processes should be critically evaluate again, since the thermal history of the sample has a strong influence on the TE properties and their evolution upon prolonged annealing. In particular significant gain in ZT for the synthetic or shaping methods implying a temperature quenching as the use of 'ribbon growth on substrate'[13,28,29] and SPS sintering[7,12,14,30] should be always examined on the long period as such gain could be only transient due to the meta-stability of phase with low γ. The fact is even more supported by the large correlation in the literature between the value of γ and the annealing temperature of the materials before quenching. From an application point of view, this needs to be taken into account when optimizing the legs geometry and predicting the long term performance of HMS-based TE generators under real application conditions.

Acknowledgements

This work was supported by the Japan Society for the Promotion of Science (grants number PE19749). TM acknowledges JST Mirai JPMJMI19A1 for support. Francis Gouttefange as is acknowledged for SEM images and EDS analyses performed on the CMEBA platform belonging to the ScanMAT unit (UMS 2001, University of Rennes 1) and which received a financial support from the European Union (CPER-FEDER 2007-2014). The authors acknowledge Bryan Briac for support work in synthesis and Christopher Hassam for writing

assistance and proofreading

References

(1) Meroz, O.; Ben-Ayoun, D.; Beeri, O.; Gelbstein, Y. Development of $Bi_2Te_{2.4}Se_{0.6}$ alloy for thermoelectric power generation applications. *J. Alloys Compd.* **2016**, *679*, 196–201.

(2) Srinivasan, B.; Le Tonquesse, S.; Gellé, A.; Bourgès, C.; Monier, L.; Ohkubo, I.; Halet, J.-F.; Berthebaud, D.; Mori, T. Screening of Transition (Y, Zr, Hf, V, Nb, Mo, Ru) and Rare-earth (La, Pr) Elements as Potential Effective Dopants for Thermoelectric GeTe – an Experimental and Theoretical Appraisal. *J. Mater. Chem. A* **2020**, *8*, 19805–19821.

(3) Ben-Ayoun, D.; Sadia, Y.; Gelbstein, Y. High temperature thermoelectric properties evolution of $Pb_{1-x}Sn_xTe$ based alloys. *J. Alloys Compd.* **2017**, *722*, 33–38.

(4) LeBlanc, S.; Yee, S. K.; Scullin, M. L.; Dames, C.; Goodson, K. E. Material and manufacturing cost considerations for thermoelectrics. *Renew. Sust. Energ. Rev.* **2014**, *84*, 313–317.

(5) Le Tonquesse, S.; Hassam, C.; Michiue, Y.; Matsushita, Y.; Pasturel, M.; Mori, T.; Suzuki, T. S.; Berthebaud, D. Crystal structure and high temperature X-ray diffraction study of thermoelectric chimney-ladder $FeGe_\gamma$ ($\gamma \approx 1.52$). *J. Alloys Compd.* **2020**, *846*, 155696.

(6) Liu, W.-D.; Chen, Z.-G.; Zou, J. Eco-Friendly Higher Manganese Silicide Thermoelectric Materials: Progress and Future Challenges. *Adv. Energy Mater.* **2018**, *8*, 1800056.

(7) Miyazaki, Y.; Igarashi, D.; Hayashi, K.; Kajitani, T.; Yubuta, K. Modulated crystal

structure of chimney-ladder higher manganese silicides $MnSi_\gamma$ ($\gamma \approx 1.74$). *Phys. Rev. B* **2008**, *78*, 214104.

(8) Van Smaalen, S. Symmetry of composite crystals. *Phys. Rev. B* **1991**, *43*, 11330–11341.

(9) Lee, H.; Kim, G.; Lee, B.; Kim, J.; Choi, S.-M.; Lee, K. H.; Lee, W. Effect of Si content on the thermoelectric transport properties of Ge-doped higher manganese silicides. *Scr. Mater.* **2017**, *135*, 72–75.

(10) Vives, S. Microstructure control and transport properties of incommensurate manganese silicide based alloys for thermoelectricity. PhD theses, Université de Bordeaux, 2015.

(11) Akselrud, L.; Cardoso Gil, R.; Wagner-Reetz, M.; Grin, Y. Disorder in the composite crystal structure of the manganese 'disilicide' $MnSi_{1.73}$ from powder X-ray diffraction data. *Acta Cryst.* **2015**, *B71*, 707–712.

(12) Kikuchi, Y.; Nakajo, T.; Hayashi, K.; Miyazaki, Y. High temperature X-ray diffraction study on incommensurate composite crystal $MnSi_\gamma$-(3+1)-dimensional superspace approach. *J. Alloys Compd.* **2014**, *616*, 263–267.

(13) Pichon, P.-Y. et al. Stability and thermoelectric performance of doped higher manganese silicide materials solidified by RGS (ribbon growth on substrate) synthesis. *J. Alloys Compd.* **2020**, 154602.

(14) Le Tonquesse, S.; Dorcet, V.; Joanny, L.; Demange, V.; Prestipino, C.; Guo, Q.; Berthebaud, D.; Mori, T.; Pasturel, M. Mesostructure - thermoelectric properties relationships in $V_xMn_{1-x}Si_{1.74}$ (x = 0, 0.04) Higher Manganese Silicides prepared by magnesiothermy. *J. Alloys Compd.* **2020**, *816*, 152577.

(15) Le Tonquesse, S.; Verastegui, Z.; Huynh, H.; Dorcet, V.; Guo, Q.; Demange, V.; Prestipino, C.; Berthebaud, D.; Mori, T.; Pasturel, M. Magnesioreduction Synthesis of Co-Doped β-$FeSi_2$: Mechanism, Microstructure, and Improved Thermoelectric Properties. *ACS Appl. Energy Mater.* **2019**, *12*, 8525–8534.

(16) Petříček, V.; Dušek, M.; Palatinus, L. Crystallographic Computing System JANA2006: General features. *Z. Kristall.* **2014**, *229*, 345–352.

(17) Stephens, P. W. Phenomenological model of anisotropic peak broadening in powder diffraction. *J. Appl. Cryst.* **1999**, *32*, 281–289.

(18) Leineweber, A.; Petříček, V. Microstrain-like diffraction-line broadening as exhibited by incommensurate phases in powder diffraction patterns. *J. Appl. Cryst.* **2007**, *40*, 1027–1034.

(19) Bérar, J.-F.; Lelann, P. E.s.d.'s and estimated probable error obtained in Rietveld refinements with local correlations. *J. Appl. Cryst.* **1991**, *24*, 1–5.

(20) Gokhale, A.; Abbaschian, G. Binary Alloys Phase Diagrams, Second Edition. **1990**,

(21) Toby, B. H. R factors in Rietveld analysis: How good is good enough? *Powder Diffr.* **2006**, *21*, 67–70.

(22) Miyazaki, Y.; Hamada, H.; Hayashi, K.; Hayashi, K. Crystal Structure and Thermoelectric Properties of Lightly Vanadium-Substituted Higher Manganese Silicides $(Mn_{1-x}V_x)Si_\gamma$. *J. Electron. Mater.* **2017**, *46*, 2705–2709.

(23) Chen, X.; Girard, S. N.; Meng, F.; Lara-Curzio, E.; Jin, S.; Goodenough, J. B.; Zhou, J.; Shi, L. Approaching the Minimum Thermal Conductivity in Rhenium-Substituted Higher Manganese Silicides. *Adv. Energy Mater.* **2014**, *4*, 1400452.

(24) Migas, D. B.; Shaposhnikov, V. L.; Filonov, A. B.; Borisenko, V. E.; Dorozhkin, N. N. Ab

initio study of the band structures of different phases of higher manganese silicides. *Phys. Rev. B* **2008**, *77*, 075205.

(25) Fredrickson, D. C.; Lee, S.; Hoffmann, R. The Nowotny Chimney Ladder Phases : Whence the 14 Electron Rule? *Inorg. Chem.* **2004**, *43*, 6159–6167.

(26) Imai, Y.; Watanabe, A. Consideration of the validity of the 14 valence electron rule for semiconducting chimney-ladder phase compounds. *Intermetallics* **2005**, *13*, 233–241.

(27) Nishida, I. Semiconducting properties of nonstoichiometric manganese silicides. *J. Mater. Sci.* **1972**, 435–440.

(28) Ghodke, S.; Sobota, R.; Berthebaud, D.; Pichon, P.-Y.; Navone, C.; Takeuchi, T. Effect of Re Substitution on the Phase Stability of Complex $MnSi_{\gamma}$. *J. Electron. Mater.* **2019**, *48*, 5827–5834.

(29) Ghodke, S.; Hiroishi, N.; Yamamoto, A.; Ikuta, H.; Matsunami, M.; Takeuchi, T. Enhanced Thermoelectric Properties of W- and Fe-Substituted $MnSi_{\gamma}$. *J. Electron. Mater.* **2016**, *45*, 5279–5284.

(30) Kikuchi, Y.; Miyazaki, Y.; Saito, Y.; Hayashi, K.; Yubuta, K.; Kajitani, T. Enhanced Thermoelectric Performance of a Chimney-Ladder $Mn_{1-x}Cr_xSi_{\gamma}$ ($\gamma \sim 1.7$) Solid Solution. *Jpn. J. Appl. Phys.* **2012**, *51*, 085801.

Graphical TOC Entry

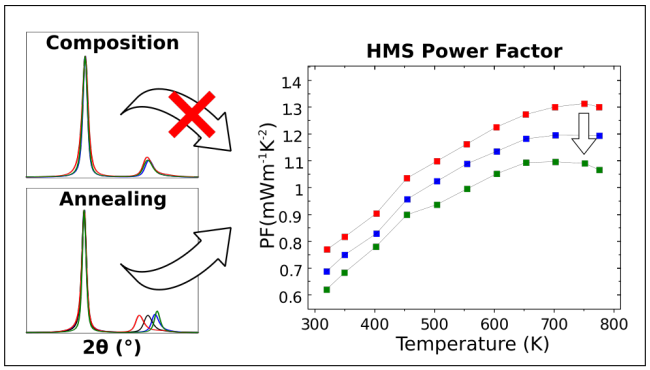

HMS power factor only depends on the annealing temperature and duration and not on the composition.